Proton-antiproton impact-electron emission spectra of He: Comparison of theory with experiment

Toru Morishita, Ken-ichi Hino, Shinichi Watanabe, and Michio Matsuzawa
Department of Applied Physics and Chemistry, The University of Electro-Communications, 1-5-1 Chofu-ga-oka, Chofu-shi, Tokyo 182, Japan
(Received 5 July 1995; revised manuscript received 13 October 1995)

We study electron emission cross sections of He decaying to $He^+(1s)$ in the $N=2$ and 3 manifolds produced by fast proton and antiproton impact. *Ab initio* close-coupling calculations are carried out using the impact-parameter method. The electronic state during collision is expanded in terms of He wave functions obtained by the hyperspherical close-coupling method. The theory reproduces experimental findings regarding both the background and doubly excited resonances well. The resonance shapes are found to depend sensitively on the sign of the projectile charge. This is due to interference between the partial waves of the ejected electron. We analyze excitation paths that eventually lead to another interference effect between continuum and doubly excited states. We demonstrate importance of both the bound and continuum states as intermediate states.

PACS number(s): 34.50.Fa, 31.50+w, 32.80.Dz

I. INTRODUCTION

Excitation and ionization of atoms by charged particles provide useful information for various applied fields such as plasma physics, radiation physics, astrophysics, etc. Of fundamental interest are the processes involving He as a target, namely excitation followed by autoionization,

$$A^{q+} + \mathrm{He} \rightarrow \mathrm{He}^{**} + A^{q+} \rightarrow \mathrm{He}^+ + e^- + A^{q+}, \qquad (1)$$

and the ionization process

$$A^{q+} + \mathrm{He} \rightarrow \mathrm{He}^{2+} + e^- + e^- + A^{q+}. \qquad (2)$$

Strictly speaking, these processes belong to the four-body problem, and probably it is safe to say that they represent the simplest of all four-body systems realizable in laboratories. What makes process (1) particularly interesting is that steady advances in experimental techniques have brought us to the point where we can even observe subtle resonant features in electron emission spectra.

On the other hand, theoretical treatment to account for every detail revealed in the experiments has long been beyond any theoretical approach despite the fact that the charge-transfer process is unimportant at the experimental energies. However, our recent work [1] as well as that of [2] proved process (1) by proton and antiproton impact to be theoretically manageable, and obtained a strong charge sign dependence in the $2l2l'$ resonance shapes. We are in a position to produce realistic theoretical cross sections and to compare them with the experiments critically.

By collision at rather high impact energies it is meant that we may regard the projectile proton as exerting a pulselike force on He so that by exploiting the accurate solution of the three-body subsystem, He, and by treating the proton as a moving source of the external field, we can calculate closely the profile of each resonance against the continuum background. (This amounts to the single-center expansion around the nucleus He^{2+} and the impact parameter method employing a straight-line trajectory for the projectile proton.) Though such a scheme for accounting for resonant profiles might appear straightforward, implementing *ab initio* calculations for real systems actually waited a while. This is partly because a reliable and flexible solution of $He^+ + e^-$ has not been readily available. Indeed, for Bachau *et al.* [3], a construction of good continuum functions seems to have been a major hindrance for setting up the close-coupled time-dependent Schrödinger equation. Though realistic continuum wave functions were not available to them, Slim *et al.* [4] instead used a simplified model to demonstrate how the use of continuum wave functions of He could produce experimentally observed features. It is actually about that time that sufficiently reliable and flexible representations of continuum wave functions came into use. One representation employs entirely time-independent hyperspherical continuum wave functions that stem from the rigorous solution of He [1], and another one uses the time-dependent Fano theory, applying a decoupling approximation that ignores the decay of doubly excited He states during collision with the projectile [2,5]. This paper is about the former representation. In this context, one must also remember efforts by other authors [6,7] who approached the problem from an independent angle, treating doubly-excited resonances as though ''discrete'' so as to obtain estimates of ''excitation'' cross sections. However, this artificial distinction of excitation and ionization processes caused some confusion in interpreting experimental cross sections [8,9]. The point is that because the ejected electron spectroscopy does not distinguish direct ionization from autoionization, it is physically impossible to extract the excitation cross section of each discrete doubly excited state. A purpose of [1] was to produce realistic theoretical electron emission cross section (EECS) in order to resolve the confusion and provide theoretical data that is directly comparable with the experiments. Martín and Salin [5] and Bordenave-Montesquieu *et al.* [10,11] noted this point likewise.

Calculating EECS using the single-center continuum wave functions of He and solving the time-dependent Schrödinger equation has thus seen a spectacular success for moderately high impact energies. However, low projectile energies where charge-transfer channels play an important role still present difficulties. Indeed, Martín and Salin [5] have shown that the single-center expansion is unsatisfactory for describing the shape parameter below 150 keV of the incident proton energy. However, an approximate representation of some charge transfer channels may enhance the validity of the procedure. We leave discussion of such an approximation to a future publication. Consequently, this paper does not explore energies below 1.5 MeV. Similarly, impact by a highly charged projectile that distorts the target states drastically is still beyond the scope. A major purpose of this paper is to examine various experimental spectra of process (1) to which our treatment is applicable and to delimit its validity as well as to check the consistency of some important experimental data.

We discuss the experimental situation on process (1). Works on this elementary process are not abundant. To our knowledge, three groups have published results of their measurements. These are Pedersen and Hvelplund [8], Giese *et al.* [9], and Bordenave-Montesquieu *et al.* [10,11]. When it comes to measurements at nonresonant energy regions, several independent data are available [12]. Each of these experiments measured the EECS as a function of the ejected electron energy and emission angle. Projectiles used are e^- and $C^{q+}(q=4-6)$ [8,9] in addition to the proton. The best experimental energy resolution is claimed to be 0.11 eV [10,11]. Hence experiments should be capable of resolving a pair of nearly coinciding resonances $2s2p\ ^1P^o$ and $(2p)^2\ ^1D^e$. Time seems thus ripe for assessing the consistency among theoretical and experimental absolute cross sections with *comparable resolution*, a rare opportunity that has become possible due to advances in experimental and theoretical technology.

This paper extends the approach to the $N=3$ manifolds from which, on account of the process of the low-lying $N=2$ manifolds, an extremely slow electron may get ejected. This phenomenon calls attention to the ionization process because the dominant configuration that contributes most to the cross section correspond to one electron slow and the other fast. Let us recall the experiment on process (2) of He by proton and antiproton impact. It has been found that the double ionization cross section by antiproton impact is about two times as large as that by proton impact at the projectile energies of a few MeV [13]. Though a calculation of this ratio was reported by Reading and Ford [14] they did not make explicit the physical mechanism responsible for this difference so that in essence we know little about the physics of double ionization by proton and antiproton impact. With a suitable generalization, the present study covering not only $N=2$ but $N=3$ manifolds may shed light on this interesting ionization problem.

This paper is organized as follows. We describe the theoretical method in Sec. II. In Sec. III, we analyze experimental and theoretical data comparing their absolute magnitudes as well as angular and energy dependence (Sec. III A). Resonance profiles are briefly examined in Sec. III B with the aid of the Shore parameters [15]. Then we move on to study experimental angular distribution in Sec. III C. The differences caused by proton and antiproton impact are studied in Sec. III D. That the impact energy is high motivated Bachau *et al.* [3] to apply the first-order Born approximation (FBA) to the time-dependent Schrödinger equation. In so doing, they made an attempt to extract the shape parameters using the FBA on $(2s)^2\ ^1S^e$, $2s2p\ ^1P^o$, and $(2p)^2\ ^1D^e$ resonances. They showed the FBA to be unreliable below 0.5 MeV of impact energies in representing the $(2s)^2\ ^1S^e$ and $(2p)^2\ ^1D^e$ resonances. The measurement of Bordenave-Montesquieu *et al.* [10] indicates that the FBA is still unsatisfactory at a high energy of about 3 MeV. This amounts to saying that the excitation and autoionization of these resonances involve higher order effects beyond the FBA even at such high experimental impact energies. We will consider the FBA in Secs. III D and III E, not for the sake of examining its validity, but as a tool for identifying dominant excitation and ionization paths. Sec. IV concludes the paper with further prospects.

II. DESCRIPTION OF THE METHOD

The principle of the method may be summarized as follows.

(1) The projectile is represented by a classical straight-line trajectory with a well-defined value of the impact parameter, thus described as a moving source of the external field.

(2) The target state wave functions of He are calculated by the hyperspherical close-coupling (HSCC) method. Thus, the autoionization mechanism is properly contained in the continuum-state wave functions.

(3) Wave-packet-type energy-discretization of the target continuum states is effected on a *flexibly chosen* energy mesh so as to evaluate the resonance profile of each resonance closely.

(4)The time-dependent Schrödinger equation is thus obtained and solved by the close-coupling (CC) method.

Below, we will describe each of the above items in some detail, supplementing the previous accounts in [1]. We note here an advantage of energy discretization in the manner of point (3) above. An alternative discretization is afforded by the L^2 basis expansion, box quantization, etc. However, it is impractical, if not impossible, to select densely populated energy mesh points around each resonance by such procedures. Hereafter, atomic units are used unless otherwise stated.

A. Classical trajectory

The position vector of the projectile is given by

$$\mathbf{X}(\mathbf{b},t)=\mathbf{b}+\mathbf{v}t, \tag{3}$$

where $\mathbf{b}$ is the impact parameter and $\mathbf{v}$ is the projectile velocity. Consequently, the potential energy term that perturbs the He target reads

$$V^{\text{p-t}}(\mathbf{r}_1,\mathbf{r}_2,\mathbf{b},t)=-\frac{Z}{|\mathbf{X}(\mathbf{b},t)-\mathbf{r}_1|}-\frac{Z}{|\mathbf{X}(\mathbf{b},t)-\mathbf{r}_2|}+\frac{2Z}{|\mathbf{X}(\mathbf{b},t)|} \tag{4}$$

for each value of impact parameter **b**, and Z is the projectile charge here. This potential leads to the scattering at each **b** so the cross section must be integrated over **b** in the end. (See Fritch and Lin [6], Moribayashi *et al.* [7] on this point.)

B. The hyperspherical close-coupling method

The He wave functions are generated by the HSCC method. This method allows us to describe the electron-electron correlation faithfully and accurately. The detailed account and accuracy check of the method have been given elsewhere [16,17]. To recapitulate the highlights, the Schrödinger equation in the hyperspherical coordinates reads

$$\left(-\frac{1}{2}\frac{\partial^2}{\partial R^2} + \frac{H_{\rm ad}^{\rm He}}{2R^2} - E \right)\varphi = 0, \tag{5}$$

where $R=\sqrt{r_1^2+r_2^2}$ is the hyperradius. φ is the rescaled wave function which is expressed as $\varphi=(R^{\frac{5}{2}}\cos\alpha\sin\alpha)\psi$, where ψ is the usual wave function corresponding to the volume element $d\mathbf{r}_1 d\mathbf{r}_2$ and $\alpha=\tan^{-1}(r_1/r_2)$ is the hyperangle. The adiabatic Hamiltonian $H_{\rm ad}^{\rm He}$ is given by

$$H_{\rm ad}^{\rm He}(R;\alpha,\hat{\mathbf{r}}_1,\hat{\mathbf{r}}_2) = \Lambda^2(\alpha,\hat{\mathbf{r}}_1,\hat{\mathbf{r}}_2) - RC(\alpha,\theta_{12}) \tag{6}$$

with

$$\Lambda^2(\alpha,\hat{\mathbf{r}}_1,\hat{\mathbf{r}}_2) = \left(-\frac{\partial^2}{\partial\alpha^2} + \frac{\mathbf{l}_1^2}{\cos^2\alpha} + \frac{\mathbf{l}_2^2}{\sin^2\alpha} \right) - \frac{1}{4} \tag{7}$$

and

$$C(\alpha,\theta_{12}) = \frac{2Z}{\cos\alpha} + \frac{2Z}{\sin\alpha} - \frac{2}{\sqrt{1-\sin 2\alpha\,\cos\theta_{12}}}. \tag{8}$$

Here, θ_{12} is the angle between $\mathbf{r}_1$ and $\mathbf{r}_2$, and $\mathbf{l}_1$ and $\mathbf{l}_2$ are angular momentum operators for the two electrons. The adiabatic Hamiltonian $H_{\rm ad}^{\rm He}$ includes both the electron-nucleus and electron-electron interaction but is devoid of derivatives with respect to R.

To solve the Schrödinger equation in the HSCC method, we first seek to expand φ in terms of orthogonal diabatic basis functions $\{\phi_\nu\}$ so that

$$\varphi = \sum_\nu F_\nu(R)\,\phi_\nu(\bar{R};\alpha,\hat{\mathbf{r}}_1,\hat{\mathbf{r}}_2), \tag{9}$$

where $\bar{R}$ is some fixed value of R appropriately chosen for each propagation sector. The function ϕ_ν is constructed as a product

$$\phi_{\lambda l_1 l_2}^{LM}(R;\alpha,\hat{\mathbf{r}}_1,\hat{\mathbf{r}}_2) = g_{\lambda l_1 l_2}^{LM}(R;\alpha)\,\mathscr{Y}_{l_1 l_2}^{LM}(\hat{\mathbf{r}}_1,\hat{\mathbf{r}}_2), \tag{10}$$

where $\mathscr{Y}_{l_1 l_2}^{LM}$ is the coupled angular momentum wavefunction of the two electrons, and additional indexes are supplemented for clarity. The function $g_{\lambda l_1 l_2}^{LM}$ is defined to be an eigenfunction of the diagonal part of the adiabatic Hamiltonian

$$\langle \mathscr{Y}_{l_1 l_2}^{LM} | H_{\rm ad}^{\rm He} | \mathscr{Y}_{l_1 l_2}^{LM} \rangle g_{\lambda l_1 l_2}^{LM}(R;\alpha) = u_{\lambda l_1 l_2}^{LM}(R)\, g_{\lambda l_1 l_2}^{LM}(R;\alpha). \tag{11}$$

Thus, $\{\phi_\nu\}$ indeed forms an orthogonal complete set at each R. This definition of $g_{\lambda l_1 l_2}^{LM}(R;\alpha)$ allows us to use an efficient and accurate numerical scheme for the 1-dimensional eigenvalue problem, and the expansion, Eq. (9), is rapidly convergent since the bulk of the radial correlations is represented by Eq. (10).

The Schrödinger equation is cast into the form of close-coupling equations by substituting (9) into (5), namely

$$-\frac{d^2}{dR^2}F_\mu(R) + \sum_\nu V_{\mu\nu}^{\rm He}(R)F_\nu(R) = 2EF_\mu(R), \tag{12}$$

where the coupling term $V_{\mu\nu}^{\rm He}(R)$ between the channel μ and ν is given by

$$V_{\mu\nu}^{\rm He}(R) = \frac{1}{R^2}\,\langle \phi_\mu(\bar{R};\alpha,\hat{\mathbf{r}}_1,\hat{\mathbf{r}}_2) | H_{\rm ad}^{\rm He} | \phi_\nu(\bar{R};\alpha,\hat{\mathbf{r}}_1,\hat{\mathbf{r}}_2)\rangle. \tag{13}$$

Solving (12) is rather standard and is described in [16]. We thus obtain the wave functions in the inner region, $R<R_M$. The wave function in the outer region, $R>R_M$, is expressed in terms of the independent-particle coordinates r_1 and r_2, that is

$$\psi_j^K = \frac{1}{r_< r_>}\sum_k \Phi_k^{\rm He^+}(r_<)\,\mathscr{Y}_{l_1 l_2}^{LM}[f_k(r_>)\,\delta_{kj} - g_k(r_>)K_{kj}], \tag{14}$$

where $r_>=\max(r_1,\,r_2)$, $r_<=\min(r_1,\,r_2)$. Here, the function $\Phi_k^{\rm He^+}$ represents the bound radial wave function of the He^+ ion. The functions f_i and g_i are the energy normalized regular and irregular radial Coulomb functions, respectively, for open channels, and exponentially increasing and decreasing functions for closed channels. The K matrix is determined by matching the set of numerical interior solutions with the set of asymptotic exterior solutions at the boundary $R=R_M$ using the two-dimensional matching procedure [16]. After evaluating the K matrix, the continuum wave functions are subjected to the incoming wave boundary condition

$$\psi_k^{(-)} = \sum_j \psi_j^K \{(iI+K)^{-1}\}_{jk}, \tag{15}$$

where I is a unit matrix. Each bound-state wave function, on the other hand, is found at an energy where $\det|K| = \infty$, that is it corresponds to the eigenvector of K with the divergent eigenvalue.

Let us realize that the solutions so obtained satisfy the two-electron Schrödinger equation rigorously to the required precision. In our later calculations, the wave functions for $^1S^e$, $^1P^o$, $^1D^e$, and $^1F^o$ symmetries are generated by using 30, 32, 35, and 18 diabatic basis functions, respectively. Table I lists our resulting bound-state energies E_B, resonance energies E_r, and widths Γ_r of the doubly excited states considered [18]. The present calculation gives almost the same energy positions and widths as those tabulated by Tang *et al.* [16] with less than a few percent difference. We also list the result by other theoretical calculations [19–23]. The agreement is sufficiently good as input for our collision calculations.

TABLE I. Energy positions $-E_B$, $-E_r$ and widths Γ_r of He below the $N=3$ threshold. $a[-b]$ means $a\times10^{-b}$.

		Other work		Present work	
States	$N(K,T)^An$	$-E_B$ (a.u.)		$-E_B$ (a.u.)	
$(1s)^2\ ^1S^e$	$1(0,0)^+1$	2.90372 [a]		2.9036	
$1s2s\ ^1S^e$	$1(0,0)^+2$	2.14597 [a]		2.1460	
$1s3s\ ^1S^e$	$1(0,0)^+3$	2.06126 [a]		2.0614	
$1s4s\ ^1S^e$	$1(0,0)^+4$	2.03356 [a]		2.0338	
$1s2p\ ^1P^o$	$1(0,0)^02$	2.12384 [a]		2.1239	
$1s3p\ ^1P^o$	$1(0,0)^03$	2.05515 [a]		2.0554	
$1s4p\ ^1P^o$	$1(0,0)^04$	2.03107 [a]		2.0313	
$1s3d^1\ D^e$	$1(0,0)^03$	2.05561 [b]		2.0559	
$1s4d^1\ D^e$	$1(0,0)^04$	2.03123 [b]		2.0315	
		$-E_r$ (Ry)	Γ_r (eV)	$-E_r$ (Ry)	Γ_r (eV)
$(2s)^2\ ^1S^e$	$2(1,0)^+2$	1.55574	1.23[-1] [c]	1.5558	1.24[-1]
$2s3s\ ^1S^e$	$2(1,0)^+2$	1.17985	3.7[-2] [c]	1.1799	3.70[-2]
$(2p)^2\ ^1S^e$	$2(-1,0)^+2$	1.24385	5.88[-3] [c]	1.2435	5.95[-3]
$(3s)^2\ ^1S^e$	$3(2,0)^+3$	0.70708	8.16[-2] [d]	0.7071	8.27[-2]
$2s2p\ ^1P^o$	$2(0,1)^+2$	1.38627	3.70[-2] [c]	1.3861	3.70[-2]
$2s3p+^1P^o$	$2(0,1)^+3$	1.1280	8.43[-3] [c]	1.1282	8.16[-3]
$2s3p-^1P^o$	$2(1,0)^-3$	1.19414	3.37[-3] [e]	1.1942	1.06[-4]
$3s3p\ ^1P^o$	$3(1,1)^+3$	0.67125	1.90[-1] [d]	0.6714	1.88[-1]
$(2p)^2\ ^1D^e$	$2(1,0)^+3$	1.40331	6.56[-2] [e]	1.4036	6.47[-2]
$2p3p\ ^1D^e$	$2(1,0)^+3$	1.13823	1.6[-2] [e]	1.1385	1.53[-2]
$2s3d\ ^1D^e$	$2(0,1)^03$	1.112806	5.41[-4] [e]	1.1129	5.43[-4]
$(3p)^2\ ^1D^e$	$3(2,0)^+3$	0.68628	1.43[-1] [d]	0.6862	1.45[-1]

[a]Reference [19].
[b]Reference [20].
[c]Reference [21].
[d]Reference [22].
[e]Reference [23].

C. Time-dependent Schrödinger equation and energy discretization

The total electronic wave function of the whole collision system is expanded by both bound-state eigenfunctions and energy-normalized continuum state eigenfunctions of He,

$$\Psi(\mathbf{r}_1,\mathbf{r}_2,\mathbf{b},t)=\sum_B C_B(\mathbf{b},t)\psi_B(\mathbf{r}_1,\mathbf{r}_2)e^{-iE_Bt} + \sum_\gamma \int_{-2}^{\infty} dE C_{E\gamma}(\mathbf{b},t)\psi^{(-)}_{E\gamma}(\mathbf{r}_1,\mathbf{r}_2)e^{-iEt}, \tag{16}$$

where B represents bound states and γ denotes a channel by a set of quantum numbers

$$\gamma=\{nl\tilde{l}LM\}, \tag{17}$$

where n and l identify the state of the He^+ ion, $\tilde{l}$ is the angular momentum of the ejected electron, and L and M represent the total angular momentum and its azimuthal component of the He atom. The expansion coefficients $C_B(\mathbf{b},t)$ and $C_{E\gamma}(\mathbf{b},t)$ of the atomic states contain all the information about the collision and satisfy the standard time dependent close-coupling equations,

$$i\frac{d}{dt}C_B=\sum_{B'}\langle\psi_B|V^{\text{p-t}}|\psi_{B'}\rangle C_{B'}e^{-i(E_B-E_{B'})t}+\sum_{\gamma'}\int_{-2}^{\infty}dE'\langle\psi_B|V^{\text{p-t}}|\psi^{(-)}_{E'\gamma'}\rangle C_{E'\gamma'}e^{-i(E_B-E')t}, \tag{18}$$

$$i\frac{d}{dt}C_{E\gamma}=\sum_{B'}\langle\psi^{(-)}_{E\gamma}|V^{\text{p-t}}|\psi_{B'}\rangle C_{B'}e^{-i(E-E_{B'})t}+\sum_{\gamma'}\int_{-2}^{\infty}dE'\langle\psi^{(-)}_{E\gamma}|V^{\text{p-t}}|\psi^{(-)}_{E'\gamma'}\rangle C_{E'\gamma'}e^{-i(E-E')t}. \tag{19}$$

These equations are solved subject to the boundary condition

$$\lim_{t\to-\infty} C_j(\mathbf{b},t)=\delta_{jB_0}, \tag{20}$$

where B_0 is the ground state of the He atom. The probability for having undergone a transition to a final state of the target, $nlm\epsilon\hat{k}$, at impact parameter $\mathbf{b}$ is obtained by summing up the expansion coefficients $C_{E\gamma}$ coherently,

$$P_{nlm\epsilon\hat{k}}(\mathbf{b})=\left|\lim_{t\to\infty}\langle\psi_{nlm\epsilon\hat{k}}e^{-iEt}|\Psi(\mathbf{r}_1,\mathbf{r}_2,\mathbf{b},t)\rangle\right|^2=\lim_{t\to\infty}\left|\sum_{\tilde{l}\tilde{m}}\sum_{LM} C_{E\gamma}(\mathbf{b},t)e^{i\sigma_{\tilde{l}}}i^{-\tilde{l}}Y_{\tilde{l}\tilde{m}}(\hat{k})\langle lm\tilde{l}\tilde{m}|LM\rangle\right|^2, \tag{21}$$

where $\epsilon=E+2/n^2$ is the electron emission energy and $\hat{k}$ is the ejection angle. Here $\sigma_{\tilde{l}}$ is the Coulomb phase shift. The probability for EECS integrated over emission angles is written as a coherent summation of the coefficients, namely,

$$P_{nl\epsilon}(\mathbf{b})=\sum_m \int d\hat{k}P_{nlm\epsilon\hat{k}}(\mathbf{b})=\sum_{\tilde{l}}\sum_{LM}|C_{E\gamma}(\mathbf{b},t)|^2. \tag{22}$$

Now, we need to approximate the integral with regard to E in Eq. (16) by a discrete sum [24]. This requires us to discretize the continuum target states of He^+ and e^-. The energy integral of Eq. (16) can be expressed as a sum of integrals by introducing a sufficiently small interval ΔE_n, and we obtain

$$\int_{-2}^{\infty} dE C_{E\gamma}(\mathbf{b},t)\psi_{E\gamma}(\mathbf{r}_1,\mathbf{r}_2)\exp(-iEt)=\sum_n \int_{E_n-\frac{1}{2}\Delta E_n}^{E_n+\frac{1}{2}\Delta E_n} dE C_{E\gamma}(\mathbf{b},t)\psi_{E\gamma}(\mathbf{r}_1,\mathbf{r}_2)\exp(-iEt)\simeq\sum_n C_{E_n\gamma}(\mathbf{b},t)\tilde{\psi}_{E_n\gamma}, \tag{23}$$

where

$$\tilde{\psi}_{E_n\gamma}=\int_{E_n-\frac{1}{2}\Delta E_n}^{E_n+\frac{1}{2}\Delta E_n} dE\,\psi_{E\gamma}(\mathbf{r}_1,\mathbf{r}_2)\exp(-iEt). \tag{24}$$

The function $\tilde{\psi}_{E_n\gamma}$ represents a wave packet which is centered about $R=k_n|t|$ and declines as $1/R$ when $|R\pm k_n t|\gg k_n/\Delta E_n$, where $R(\simeq r_>)$ is the hyperradius and k_n is the magnitude of ejected electron momentum. If $|R\pm k_n t|<k_n/\Delta E_n$ and $\Delta E_n\ll k_n^2$, the packet $\tilde{\psi}_{E_n\gamma}$ can be approximately described by the representative component $\psi_{E_n\gamma}$ of that interval. This decline of $\tilde{\psi}_{E_n\gamma}$ as $1/R$ ensures that the continuum-continuum coupling term

$$\langle\tilde{\psi}_{E_n\gamma}|V^{\text{p-t}}|\tilde{\psi}_{E_{n'}\gamma'}\rangle \tag{25}$$

is always finite; this statement includes the case $E_n=E_{n'}$ even though the original matrix element

$$\langle\psi_{E\gamma}|V^{\text{p-t}}|\psi_{E'\gamma'}\rangle \tag{26}$$

is divergent at $E\simeq E'$ owing to the long-range Coulomb interaction [25]. Carrying out the energy integration before the spatial integration has a drastic influence on the collision calculation. To be more precise, it can be shown that if an incident particle is faster than an ejected electron, the contribution from the asymptotic electron distances drops out upon the energy integration [25]. Therefore, it is sufficient to consider a finite region near the target for evaluating the matrix element. This motivates us to introduce the convergence factor η, that is we replace V^{p-t} by $V^{p-t}\exp(-\eta R)$ in calculating the matrix elements between continuum wave packets.

The expansion coefficients in the FBA is obtained by substituting the zero order approximation, $C_j(\mathbf{b},t)=\delta_{jB_0}$, in the right hand side of Eqs. (18) and (19) and integrating with respect to t, namely,

$$C_B(\mathbf{b},t)=-i\int_{-\infty}^{t} dt\langle\psi_B|V^{\text{p-t}}|\psi_{B_0}\rangle e^{-i(E_B-E'_{B_0})t}, \tag{27}$$

$$C_{E\gamma}(\mathbf{b},t)=-i\int_{-\infty}^{t} dt\langle\psi_{E\gamma}^{(-)}|V^{\text{p-t}}|\psi_{B_0}\rangle e^{-i(E-E'_{B_0})t}. \tag{28}$$

It is clear that the cross sections by the FBA scale linearly with Z^2.

III. ANALYSIS OF THEORETICAL AND EXPERIMENTAL CROSS SECTIONS

Table II indicates the atomic states adopted as the basis set together with the range of energy and the number of energy mesh points. We have chosen the energy range of continuum states from the first ionization threshold -2 a.u. up to -0.32 a.u. for $^1S^e$, $^1P^o$, and $^1D^e$ symmetries, and -2 a.u. to -0.5 a.u. for $^1F^o$. Note both ranges cover below the $(3p)^2\ ^1S^e$ state. We concentrate the energy mesh around the resonances of interest and neglect the contribution from higher energy states because the associated matrix elements are small and cause negligibly small effects.

The factor η helps to accelerate the convergence of the integral, Eq. (25), as a function of the upper integration limit

TABLE II. Target states used for expanding the collision system.

	Bound states	Continuum states	
	States	Energy range (a.u.)	No. of energy mesh points
$^1S^e$	$(1s)^2$, $1s2s$, $1s3s$, $1s4s$	$-2\sim-0.32$	145
$^1P^o$	$1s2p$, $1s3p$, $1s4p$	$-2\sim-0.32$	177
$^1D^e$	$1s3d$, $1s4d$	$-2\sim-0.32$	157
$^1F^o$		$-2\sim-0.5$	38

with respect to R. In the actual numerical calculations, we set η to be 0.04 a.u. Since this value of η is so small that it does not affect the resonant state wave functions that are localized within about 10 a.u. The calculated cross sections are found stable, and depend smoothly on energy. For the states below the $N=2$ threshold, the cross section at a fixed energy is constant within a relative error of a few % when η is varied from 0.1 to 0.04. On the other hand, we found a slower convergence for $3l3l'$ states whose wave functions extend more broadly. We note the largest relative difference between the results at $\eta=0.04$ and 0.08 is about 20% near the $(3p)^2\ ^1D^e$ resonance position.

Let us define Shore parameters [15] which serve to summarize physiognomic features of the electron emission spectrum near isolated autoionizing resonances, namely,

$$\frac{d\sigma}{d\epsilon d\Omega}=F(\epsilon,\theta)+\sum_r \frac{A_r(\theta)\varepsilon_r+B_r(\theta)}{1+\varepsilon_r^2}, \qquad (29)$$

where $F(\epsilon,\theta)$ is the background at the emission energy ϵ, and $\varepsilon_r=2(\epsilon-\epsilon_r)/\Gamma_r$ is the normalized electron energy. The Shore parameters A_r and B_r are said to contain information concerning collision dynamics, and may be defined for each emission angle, that is we regard A_r and B_r as functions of θ in general. We determine these parameters by the least-square fitting of formula (29) to the calculated spectra, assuming the background cross section to be linear in energy, namely $F^0(\theta)+F^1(\theta)\epsilon$, and employing the resonance positions and widths determined for an isolated He. Martín and Salin obtain the θ-dependent Shore parameters without fitting [26]. For this to be possible, they assume instead that during the collision with the projectile the isolated He does not undergo autoionization. Our use of the resonance positions and widths of the isolated He is in a rather loose sense, of the same spirit as theirs, and helps to stabilize the fitting procedure.

First, we present unconvoluted raw theoretical EECS at $\theta=20°$, 90°, and 150° in Figs. 1(a), 1(b), and 1(c), respectively at the proton impact energy of 3 MeV, as a first example. The pronounced structures are due to the $2l2l'$ and $2l3l'$ resonances. The $3l3l'$ resonance structures in the $He^+(1s)+e^-$ continuum channel appear above 40.8 eV of the $N=2$ threshold of He^+. Though there exist other decay channels for $3l3l'$ resonances, namely $He^+(2s,2p)+e^-$, we do not touch on this in the present paper. One general feature we observe from this result is that the shape of each resonance reflects the correlation patterns. Thus the resonances belonging to the same hyperspherical channel share all the correlation quantum numbers and reveal very similar line profiles. For example, the $2s2p\ ^1P^o$ and $2s3p+^1P^o$

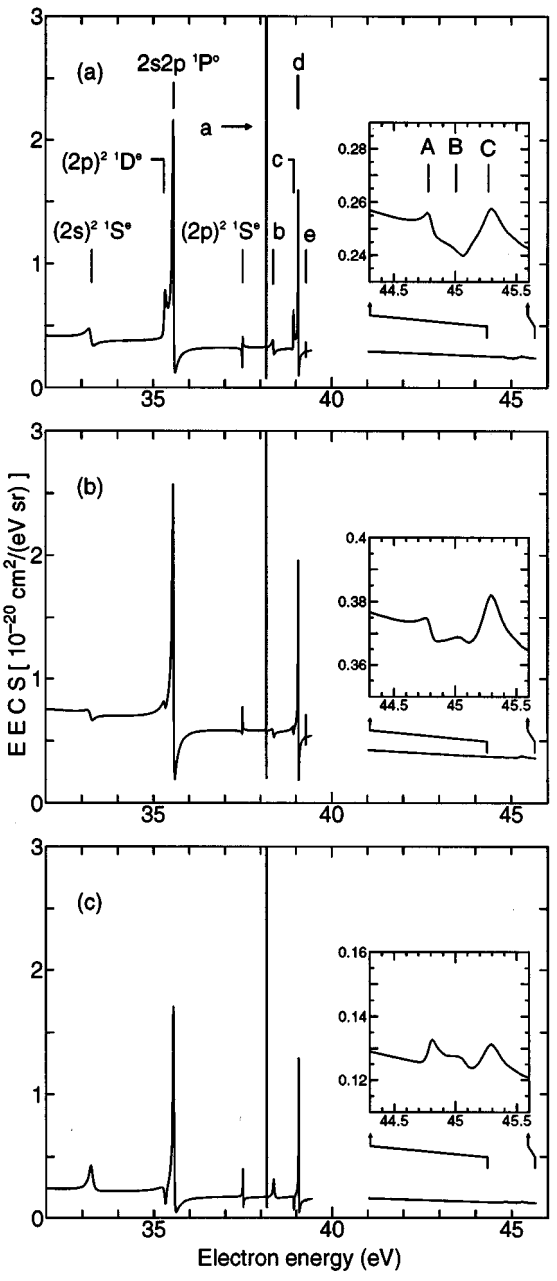

FIG. 1. Calculated electron emission cross section of He by 3 MeV proton impact at (a) 20°, (b) 90°, and (c) 150°. To avoid cluttering, the energy positions of the lower-lying doubly excited states are indicated in (a). The higher-lying states are indicated as a=$2s3p-^1P^o$; b=$2s3s\ ^1S^e$; c=$2p3p\ ^1D^e$; d=$2s3p+^1P^o$; e=$2s3d\ ^1D^e$; A=$(3S)^2\ ^1S^e$; B=$3s3p\ ^1P^o$; C=$(3p)^2\ ^1D^e$.

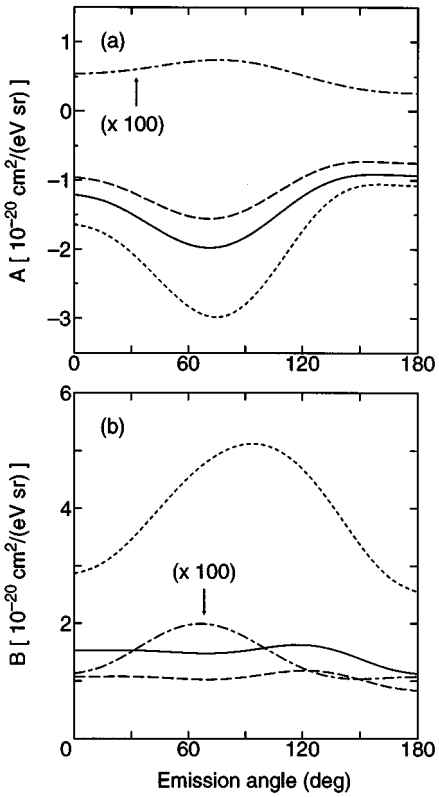

FIG. 2. Shore parameters (a) A and (b) B of the $2s2p\ ^1P^o$ (solid line), $2s3p+^1P^o$ (dashed line), $2s3p-^1P^o$ (dotted line), and $3s3p\ ^1P^o$ (dashed dotted line) resonances for 3 MeV proton impact.

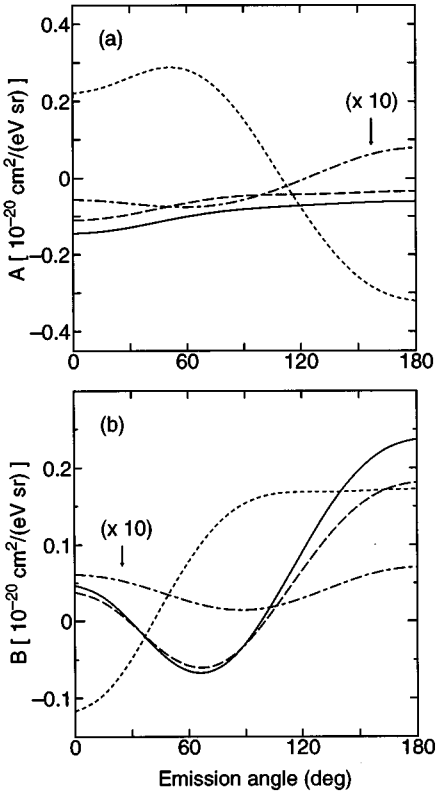

FIG. 3. Shore parameters (a) A and (b) B of the $(2s)^2\ ^1S^e$ (solid line), $2s3s^1\ S^e$ (dashed line), $(2p)^2\ ^1S^e$ (dotted line), and $(3s)^2\ ^1S^e$ (dashed dotted line) resonances for 3 MeV proton impact.

resonances, i.e., $A=+$, are prominent peaks followed by marked dips on the higher end (see [18]). Figures 2(a) and 2(b) supplement this point. It shows the Shore parameters for the $2s2p\ ^1P^o$, $2s3p+^1P^o$, $2s3p-^1P^o$, and $3s3p^1\ P^o$ resonances. The angular dependence of the Shore parameters for the $2s2p^1\ P^o$ and $2s3p+^1P^o$ shows a close resemblance. The $^1S^e$ and $^1D^e$ resonances show a similar tendency (Figs. 3 and 4). Another important observation is that the resonance profile of some resonances, typically the $^1S^e$ and $^1D^e$ resonances, is a rather sharp function of the emission angle; their profiles in Fig. 1(a) are completely reversed in Fig. 1(c) (see also Figs. 3 and 4). This conspicuous interference effect is a signature of the 4-body problem and may be shared in collisions with other projectiles such as an electron. We will return to a more rigorous discussion on the resonance profile later with the Shore parameters. In comparing with experiments, we deal with our theoretical data convoluted with the resolution of each measurement. We will then focus on the absolute magnitude of the cross section at several emission angles and energies as well as on clearly discernible resonant features. Note that the impact energy will not be restricted to 3 MeV in the following analysis, but the general features of the EECS as described above are not strongly dependent on the impact energy in the range of 1 MeV to 3 MeV.

A. Absolute cross section and its angular and energy dependence

Since the theoretical method is capable of evaluating absolute cross sections, we first consider the magnitude of the nonresonant background cross sections. The main contribution to the energy-integrated cross section derives from this background part, and its reproduction is tantamount to examining, on the one hand, the choice of adequate energy mesh points that affect the numerous state-to-state couplings, and on the other hand, and perhaps more importantly, the components of higher angular momentum $\tilde{l}$ of the ejected electron. Note $\tilde{l}$ is equal to the total angular momentum L of the final states in the case of $He^+(1s)+e^-$. The resonant part of a cross section is also of importance in checking the absolute magnitude, but it is more subtly affected by interference between doubly excited and continuum states than the background, so its analysis will be done separately in the context of resonance profiles.

In Figs. 5(a)–5(c), the calculated EECS at the proton impact energy of 1.5 MeV and the ejected electron energy of 10, 20, and 30 eV are shown as functions of the emission angle. We also show by dashed lines the results that exclude the $L=3$ states in the close-coupling calculation. We see from these figures that the inclusion of the $L=3$ states shift the position of the maximum to the backward direction, i.e., toward larger angles of θ, and increases its peak value. In the backward direction, the results with $L=3$ states lower than those without, that is the more converged the result is the less marked the dip is at $\theta\sim120°$. Further, the contribution from the $L=3$ states become larger when the ejected electron energy increases. At 10 eV of ejected electron energy, even the result excluding the $L=3$ states show satisfactory convergence, and almost coincide with experiment. However, the result $L=3$ included falls still about 10% lower than the

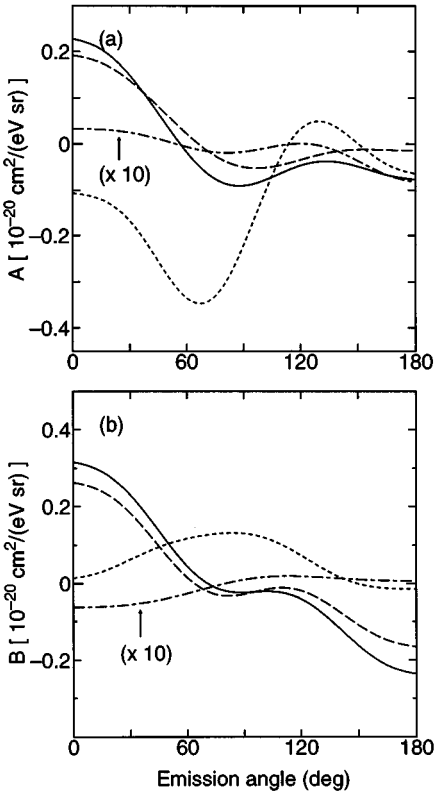

FIG. 4. Shore parameters (a) A and (b) B of the $(2p)^2\ ^1D^e$ (solid line), $2p3p\ ^1D^e$ (dashed line), $2s3d\ ^1D^e$ (dotted line), and $(3p)^2\ ^1D^e$ (dashed dotted line) resonances for 3 MeV proton impact.

experiment at around the peak at 30 eV. We also compare with the measurement by Giese *et al.* Figures 6(a)–6(c) show a comparison at $\theta = 10°$, 20°, and 40°. It indicates indeed an excellent agreement attained for the background in the energy range up to 35 eV. Beyond this energy, the theoretical background is about 5% to 10% lower than the experiment. Note, however, that the experimental errors are about 20% throughout [27]. The seeming discrepancy thus tends to grow larger for higher emission energies, while the agreement at the lowest emission energy of 10 eV in Fig. 5(a) is excellent. This observation on the energy and angle dependence suggests lack of higher angular momentum components $L(=\tilde{l})$ of the ejected electron. The pattern of discrepancy is similar in a comparison with other experiments at different incident energies (Figs. 7 and 8). The subtraction of noise from the experimental data may as well play some part in the difference. Unfortunately, including higher angular momentum components in the present treatment is beyond the capacity of our current computing facility (IBM RS6000/350 with 96 Mb of main memory and 200 Mb of disk space for this run). Of course, there also remains the possibility of systematic experimental errors. Bordenave-Montesquieu *et al.* [11] shows a similar pattern of discrepancy. (See Fig. 3 of [11]. To avoid confusion, let us note that they superimposed experimental and theoretical cross sections near resonances deduced from Shore parameters. The energy positions and the magnitude of the background may not necessarily coincide with Figs. 4 and 5 therein [28].) Despite some marginal differences noted above, the agreement in the absolute magnitude is excellent. No other theory in the past, with the exception of Martín and Salin [5], has achieved anything close to this level of agreement.

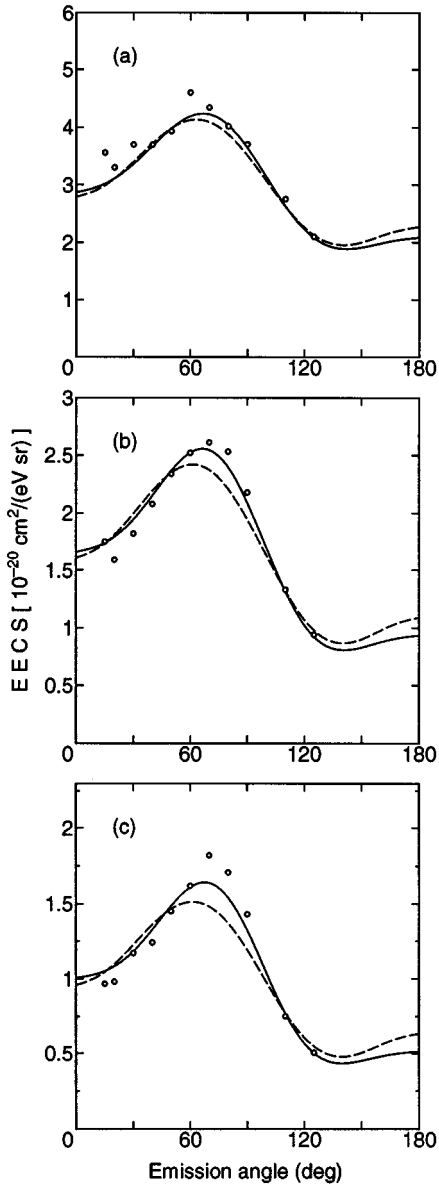

FIG. 5. Comparison of experimental and theoretical angular dependence of electron emission cross sections of He at emission energies of (a) 10 eV, (b) 20 eV, and (c) 30 eV by 1.5 MeV proton impact. Solid line: present calculation with $L=3$ states. Dashed line: present calculation without $L=3$ states. Open circles: experimental result of Rudd *et al.* [12].

B. Resonance profiles

Next, let us consider doubly excited resonances. These resonances are produced as a result of rather strong radial and angular correlations. The shape parameters depend sensitively on the interference of various terms and thus provide a good signature of every resonance.

Let us return to the observation that concerns the dependence of shape parameters on the emission angle. Let us recall that the $^1S^e$ and $^1D^e$ resonances show marked dependence whereas the $^1P^o$ resonances are insensitive to the

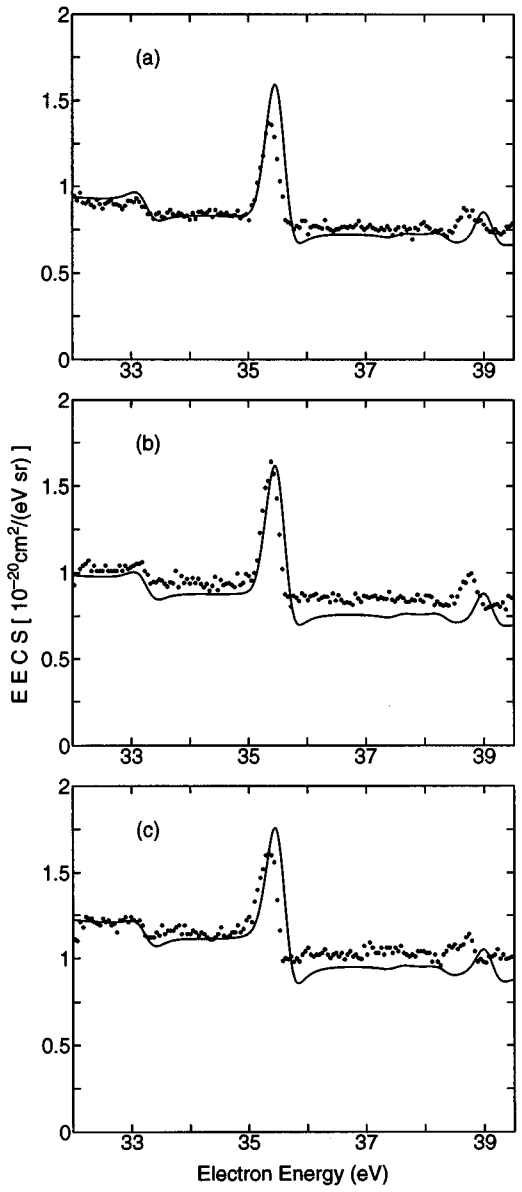

FIG. 6. Comparison of experimental and theoretical electron emission cross sections of He with 1.5 MeV proton impact at (a) 10°, (b) 20°, and (c) 40°. Experimental results of Giese *et al.* [9] are shown by dots. The solid lines are our theoretical results convoluted with a resolution of 0.3 eV for comparison.

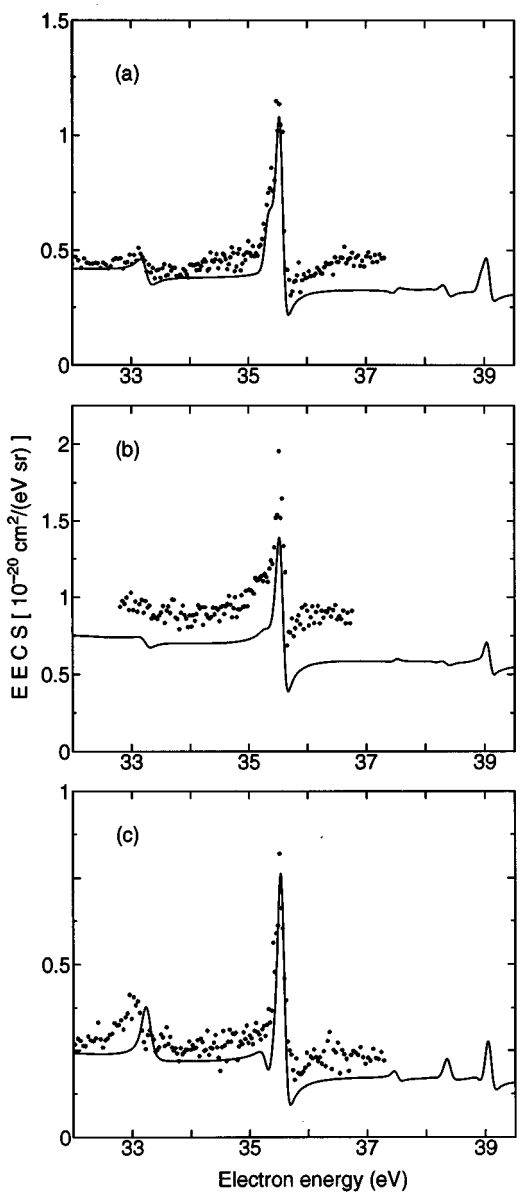

FIG. 7. Comparison of experimental and theoretical electron emission cross sections of He with 3 MeV proton impact at (a) 20°, (b) 90°, and (c) 150°. Experimental results of Bordenave-Montesquieu *et al.* [10] are shown by dots. The solid lines are our theoretical results convoluted with a resolution of 0.11 eV for comparison.

variation of the angle. This sharp dependence of the $^1S^e$ and $^1D^e$ resonances is clearly reflected in Figs. 3 and 4. The Shore parameters of the $^1P^o$ resonance is indeed weakly dependent on θ. Let us recall that the resonance line shape emerges as a result of the interference of various partial waves. (This point will be made more explicit later through the study of EECS by antiproton impact.) One possible interpretation of this observation is that the relative phase between the resonance and the continuum background is markedly different for the $^1S^e$ and $^1D^e$ states. The verification of this requires us to read off this relative phase from the expansion coefficients C in Eq. (16) and the spherical harmonics. A systematic analysis of this relative phase requires us to identify relevant theoretical parameters. This task is postponed until future investigation.

C. Experimental angular distribution

In comparing with the experimental EECS, we must convolute our theoretical one. We do so first with the cross section of Bordenave-Montesquieu *et al.* in Fig. 7. Their data are limited mainly to the $2l2l'$ doubly excited resonances. The Gaussian convolution is carried out with the reported experimental resolution of 0.11 eV. Therefore the narrow resonances $2s3p-{}^1P^o$ and $2s3d\ {}^1D^e$ with $A=-$ and 0 become smoothed out. The $A=+$ type resonances are broad enough to remain visible after convolution. The convoluted theoretical cross sections agree with experimental ones excellently at $\theta=20°$ and 150°. However, as noted earlier in connection with Fig. 5, the disagreement grows to about 30∼40% at 90° though still this falls within the bounds of

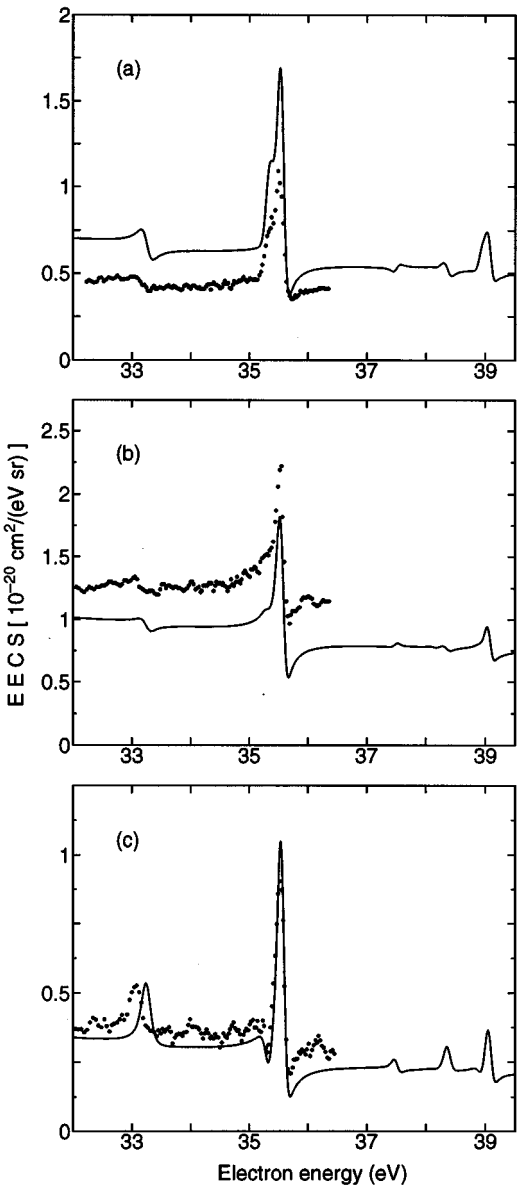

FIG. 8. Comparison of experimental and theoretical electron emission cross sections of He with 2 MeV proton impact at (a) 20°, (b) 90°, and (c) 150°. Experimental results of Bordenave-Montesquieu *et al.* [11] are shown by dots. The solid lines are our theoretical results convoluted with a resolution of 0.11 eV for comparison.

the reported error of $\pm 35\%$. The scattering of the experimental data is admittedly large. The $(2p)^2\ ^1D^e$ resonance that manifests itself as a minor shoulder at the left side of the $2s2p\,^1P^o$ in the theoretical curve appears very vaguely in the experimental data. Without statistical analysis carried out on the experimental data, this stands as a mere impression. The experiment may require better statistics.

Next, we compare with the cross sections at impact energy of 2 MeV in Fig. 8. The general features are similar to the EECS at 3 MeV except for the discrepancy in magnitude of background at 20°. An obviously unsatisfactory feature is the sharp dip which is visible at the right side of the $2s2p\ ^1P^o$ resonance in the theoretical cross section. On the other hand, it is almost smoothed out in the experiment at the smallest angle of 20°. The other theory produces a similar dip [11]. Bordenave-Montesquieu *et al.* suggest that the post collision interaction (PCI) effects [29–32] may play a role even at such a high incident energy [11]. Further theoretical work including the PCI as well as charge transfer effects [36] is necessary to clarify this point.

One aspect that appears seriously unsatisfactory on the part of the experiments is energy calibration. In the experiments of Bordenave-Montesquieu *et al.* [10,11], energy is referenced to the $2s2p\ ^1P^o$ resonance, so the $(2s)^2\ ^1S^e$ resonance located about 3.5 eV lower in energy becomes noticeably shifted from the theoretical one which is at 33.251 eV (see Table III). Experimental energy calibration needs improvement.

We omit comparison of the shapes with other experiments because they are of considerably less resolution and yield at present no additional information, although they played an important historical role in the field. Nonetheless, it is worth mentioning that Giese *et al.* carried their measurement to a greater length in electron emission energy reaching about 43 eV which is above the $He^+(N=2)$ thresholds, but below the $3l3l'$ resonances. Our calculations show that the line shape of the third lowest $2s3p+^1P^o$ resonance is more or less properly reproduced but other resonances nearby are all smeared and that their energy calibration is off by about 0.3 eV at the highest end of our calculation in this paper $\sim$39 eV (Fig. 6).

D. Electron emission cross section for proton and antiproton impact

We consider the dependence of EECS on the sign of the projectile charge. It gives a first glimpse at the complexity of various excitation mechanisms, but also some hint as to how to separate and interpret the transition processes. In order to make the dependence on the charge explicit, we denote by Z the projectile charge $Z=\pm 1$. We show EECS for 3-MeV proton and antiproton impact in Figs. 9 and 10. In an earlier work, we found the shape of the $(2p)^2\ ^1D^e$ state depended markedly on the sign of Z at impact energy of 1.5 MeV [1]. Even at 3 MeV, this striking dependence holds for the resonance shapes of $(2p)^2\ ^1D^e$, $2p3p\ ^1D^e$, $(2p)^2\ ^1S^e$, $2s3d\ ^1D^e$, and $(3p)^2\ ^1D^e$ which we shall call hereafter type-II states. These states are primarily reached by two-step dipole transition. (In cases of $2s3d\ ^1D^e$ and $(3p)^2\ ^1D^e$, there seems to be some contribution from other transitions.) This point will be further illuminated later. On the other hand, the shapes of $(2s)^2\ ^1S^e$, $2s3s\ ^1S^e$, $2s2p\ ^1P^o$, $2s3p+^1P^o$, $2s3p-^1P^o$, $(3s)^2\ ^1S^e$, and $3s3p\ ^1P^o$states, called hereafter type-I states, remain nearly unaltered regardless of whether proton or antiproton is used for impact. The type-I states are reached either by direct monopole transition or by one-step dipole transition. This difference in the mechanism of exciting type-I and type-II resonances may be simply explained as follows. In order to connect the present result with a perturbative picture, we employ the result by the FBA and compare with that by the CC method. Now we argue that type-I states are mainly produced by first-order process which scales linearly with Z^2, while higher-order processes which scale like Z^4 contribute largely to type-II states. Meanwhile the background cross section is due to a

TABLE III. Calculated values of the Shore parameters in cm^2/eV of $2lnl'$ and $3l3l'$ resonances decaying to $He^+(1s)$ at an incident energy of 3 MeV. The first line of each entry is the result for proton impact (p), the second line is for antiproton impact ($\overline{\text{p}}$), and the third line is the first Born approximation (FBA). $a[-b]$ means $a\times10^{-b}$.

	$\mathscr{F}^0$	$\mathscr{F}^1$	$\mathscr{A}_r$	$\mathscr{B}_r$
	$(2s)^2\ ^1S^e$, ϵ_r=33.251 eV, Γ_r=0.124 eV			
p	8.35[-21]	-1.18[-22]	-1.05[-20]	3.17[-21]
$\overline{\text{p}}$	8.35[-21]	-1.23[-22]	-9.89[-21]	2.71[-21]
FBA	8.26[-21]	-1.18[-22]	-1.07[-20]	2.54[-21]
	$(2p)^2\ ^1S^e$, ϵ_r=37.500 eV, Γ_r=0.00595 eV			
p	8.35[-21]	-1.18[-22]	1.23[-20]	1.40[-20]
$\overline{\text{p}}$	8.35[-21]	-1.23[-22]	1.17[-20]	1.44[-20]
FBA	8.26[-21]	-1.18[-22]	1.06[-20]	3.17[-21]
	$2s3s\ ^1S^e$, ϵ_r=38.364 eV, Γ_r=0.0370 eV			
p	8.35[-21]	-1.18[-22]	-8.27[-21]	2.29[-21]
$\overline{\text{p}}$	8.35[-21]	-1.23[-22]	-7.77[-21]	2.06[-21]
FBA	8.26[-21]	-1.18[-22]	-8.33[-21]	1.93[-21]
	$(3s)^2\ ^1S^e$, ϵ_r=44.796 eV, Γ_r=0.0827 eV			
p	6.37[-21]	-7.98[-23]	-4.68[-22]	4.01[-22]
$\overline{\text{p}}$	5.73[-21]	-7.31[-23]	-9.46[-22]	1.87[-22]
FBA	5.93[-21]	-7.45[-23]	-7.29[-22]	3.32[-22]
	$2s2p\ ^1P^o$, ϵ_r=35.559 eV, Γ_r=0.0370 eV			
p	1.09[-19]	-1.85[-21]	-1.93[-19]	1.92[-19]
$\overline{\text{p}}$	1.07[-19]	-1.81[-21]	-1.92[-19]	1.89[-19]
FBA	1.08[-19]	-1.83[-21]	-1.96[-19]	1.91[-19]
	$2s3p-\ ^1P^o$, ϵ_r=38.170 eV, Γ_r=0.000106 eV			
p	1.09[-19]	-1.85[-21]	-2.72[-19]	5.54[-19]
$\overline{\text{p}}$	1.07[-19]	-1.81[-21]	-2.85[-19]	6.22[-19]
FBA	1.08[-19]	-1.83[-21]	-2.84[-19]	5.85[-19]
	$2s3p+\ ^1P^o$, ϵ_r=39.067 eV, Γ_r=0.00816 eV			
p	1.09[-19]	-1.85[-21]	-1.52[-19]	1.36[-19]
$\overline{\text{p}}$	1.07[-19]	-1.81[-21]	-1.52[-19]	1.37[-19]
FBA	1.08[-19]	-1.83[-21]	-1.55[-19]	1.36[-19]
	$3s3p\ ^1P^o$, ϵ_r=45.281 eV, Γ_r=0.188 eV			
p	8.01[-20]	-1.18[-22]	-6.71[-22]	1.95[-21]
$\overline{\text{p}}$	8.05[-20]	-1.20[-22]	-7.27[-24]	2.29[-21]
FBA	8.16[-21]	-1.22[-22]	-3.51[-22]	2.15[-21]
	$(2p)^2\ ^1D^e$, ϵ_r=35.321 eV, Γ_r=0.0647 eV			
p	1.71[-20]	-2.29[-22]	-2.67[-21]	8.36[-22]
$\overline{\text{p}}$	1.72[-20]	-2.42[-22]	-2.52[-21]	9.43[-22]
FBA	1.68[-20]	-2.27[-22]	-4.56[-21]	-7.58[-21]
	$2p3p\ ^1D^e$, ϵ_r= 38.928 eV, Γ_r=0.0153 eV			
p	1.71[-20]	-2.29[-22]	-2.80[-22]	-2.80[-22]
$\overline{\text{p}}$	1.72[-20]	-2.42[-22]	-3.23[-22]	-4.91[-22]
FBA	1.68[-20]	-2.27[-22]	-2.24[-21]	-7.03[-21]

TABLE III. (*Continued*).

	$\mathscr{F}^0$	$\mathscr{F}^1$	$\mathscr{A}_r$	$\mathscr{B}_r$
		$2s3d\ ^1D^e$, ϵ_r=39.275 eV, Γ_r=0.000543 eV		
p	1.71[-20]	-2.29[-22]	-1.89[-20]	9.55[-21]
$\overline{\text{p}}$	1.72[-20]	-2.42[-22]	-1.71[-20]	8.17[-21]
FBA	1.68[-20]	-2.27[-22]	-1.97[-20]	5.39[-21]
		$(3p)^2\ ^1D^e$, ϵ_r=45.081 eV, Γ_r=0.145 eV		
p	1.36[-20]	-1.48[-22]	-1.95[-22]	-1.21[-22]
$\overline{\text{p}}$	1.36[-20]	-1.67[-22]	-7.73[-22]	7.27[-23]
FBA	1.37[-20]	-1.62[-22]	-5.03[-22]	3.67[-24]

one-step transition. Consequently, there emerges a Z^3 term representing interference between a type-II resonance and the background as a result of summing the expansion coefficients over the angular momentum L and M coherently [see Eq. (21)]. Therefore differences in the EECS at a fixed angle appear for particles of opposite charges near the resonances of type-II states.

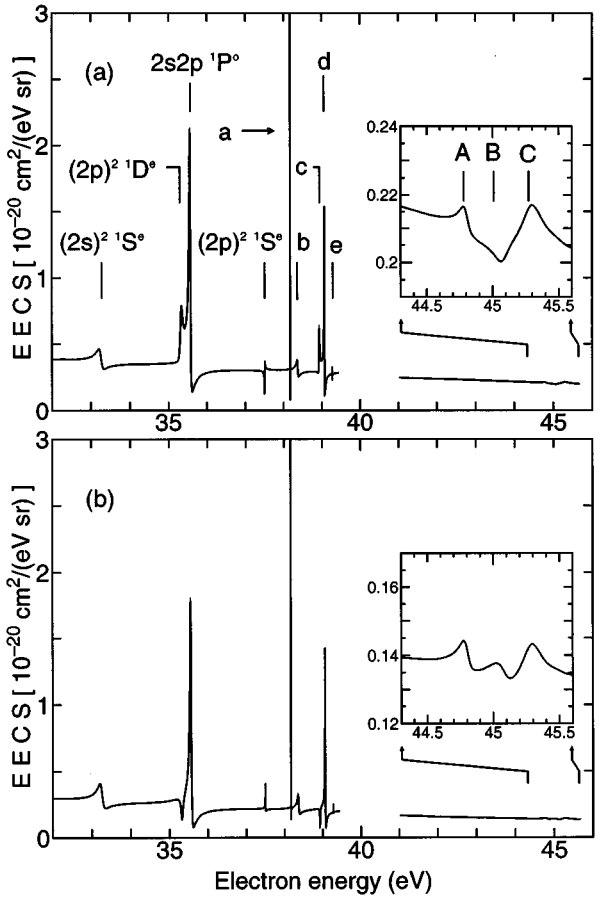

FIG. 9. Calculated electron emission cross section of He with 3 MeV (a) proton and (b) antiproton impact at 0°. To avoid cluttering, the energy positions of the lower-lying doubly excited states are indicated in (a). The higher-lying states are indicated as a=$2s3p-{}^1P^o$; b=$2s3s\ ^1S^e$; c=$2p3p\ ^1D^e$; d=$2s3p+{}^1P^o$; e=$2s3d\ ^1D^e$; A=$(3s)^2\ ^1S^e$; B=$3s3p\ ^1P^o$; C=$(3p)^{21}D^e$.

Next, we analyze EECS integrated over the emission angle which becomes devoid of the interference terms between different partial waves. The collision dynamics can thus be separately analyzed for each resonance identified by the total atomic angular momentum L and M [see Eq. (22)]. The angle-integrated EECS is also described by the Shore formula,

$$\frac{d\sigma}{d\epsilon}=\mathscr{F}(\epsilon)+\sum_r \frac{\mathscr{A}_r\varepsilon_r+\mathscr{B}_r}{1+\varepsilon_r^2}. \tag{30}$$

The study of excitation mechanism with the aid of $\mathscr{A}_r$ and

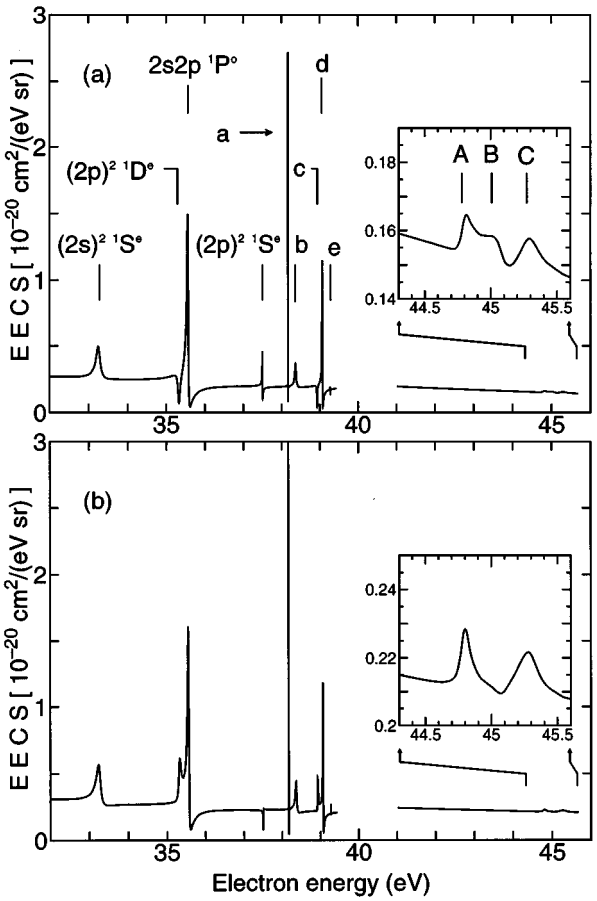

FIG. 10. Same as in Fig. 9 but for the emission angle of 180°.

TABLE IV. Calculated values of the Shore parameters in cm^2/eV for the $(2p)^2\ ^1D^e$ resonance at 3 MeV proton impact energy. Line (1) is the result of a calculation without truncation, (2) is the first Born approximation. (3)–(6) indicate the calculated parameters with the following state(s) excluded: (3) $1s2p$ and $1s\epsilon p$; (4) low $1s\epsilon p$; (5) middle $1s\epsilon p$; (6) high $1s\epsilon p$ (see text). $a[-b]$ means $a\times10^{-b}$.

	$\mathscr{F}^0$	$\mathscr{F}^1$	$\mathscr{A}_r$	$\mathscr{B}_r$
(1)	1.71[-20]	-2.29[-22]	-2.67[-21]	8.36[-22]
(2)	1.68[-20]	-2.27[-22]	-4.56[-21]	-7.58[-21]
(3)	1.68[-20]	-2.32[-22]	-4.49[-21]	-7.37[-21]
(4)	1.66[-20]	-2.18[-22]	-3.42[-21]	-3.16[-21]
(5)	1.58[-20]	-2.01[-22]	-3.91[-21]	-2.05[-22]
(6)	1.86[-20]	-2.74[-22]	-3.66[-21]	-6.67[-23]

$\mathscr{B}_r$ is the main objective of this subsection. As demonstrated at the beginning of this section, we continue to determine the parameters $\mathscr{A}_r$ and $\mathscr{B}_r$ by applying the least-square fitting to our resulting spectra assuming a linear background function $\mathscr{F}^0+\mathscr{F}^1\epsilon$.

The parameters of the $2lnl'$ and $3l3l'$ resonances decaying to $He^+(1s)$ for the 3-MeV proton and antiproton impact are shown in Table III. The parameters for the FBA are also given in the same table. It is found that the results of type-I states by the FBA almost coincide with that by the CC calculations, because the excitation of these resonances proceed primarily by a monopole or a dipole transition as argued above. On the other hand, there are large departures in the case of type-II states. Therefore the higher order processes are indeed seen to play a significant role in the excitation to type-II states. From Table III, we also find that the proton impact case and the antiproton impact case both yield similar shape parameters as they should since the interference between partial waves drop out upon the angular integration. Indeed, according to our result, the coefficient of Z^3 term is much smaller than those of the Z^2 and Z^4 terms. Martín and Salin reported a similar result for $(2s)^2\ ^1S^e$ and $(2p)^2\ ^1D^e$ states [2].

We similarly analyzed EECS cross sections at the proton impact energy of 2 MeV. No substantial difference from those at 3 MeV is found. So we do not touch on the 2-MeV proton impact in this paper.

E. Identifying excitation paths

For enhancing our understanding of the excitation mechanism, we investigate the role of intermediate states. The previous coupled-channel studies [6,7] analyzed the double electron excitation processes by masking particular intermediate states in the evaluation of the cross sections. Technically, this masking is done by excluding some intermediate states. When the difference between the cross sections with and without the intermediate states is large, we identify them as important intermediate states.

Moribayashi *et al.* found that the discrete $2s2p\ ^1P^o$ doubly excited state as well as the $1s2p\ ^1P^o$ singly excited state plays an essential role in the excitation to the $(2p)^2\ ^1D^e$ state. Such an analysis is, however, incomplete, the interference of the continuum states and doubly excited states being essential (see Sec. I). Indeed, the major contributors to double excitation are intermediate states of the type $1s\epsilon p\ ^1P^o$, etc., We wish to verify this point below, concentrating on the excitation mechanism to the $(2p)^2{}^1D^e$ resonance, whose cross section shows the largest variation from proton to antiproton impact [37].

The Shore parameters for the $(2p)^2\ ^1D^e$ resonance are listed in Table IV for some intermediate states masked out. The parameters calculated with exclusion of the $1s2p\ ^1P^o$ singly excited state and the $1s\epsilon p\ ^1P^o$ continuum states are almost equal to the FBA results, thus differing considerably from the full cross section. Hence, these states have predominant contribution as intermediate states. To analyze the effects of the continuum states in detail, we also evaluate the parameters, excluding "low-," "middle-," and "high-" energy portions of the $1s\epsilon p$ continuum states listed in Table IV. The low $1s\epsilon p\ ^1P^o$ consists of the discretized continuum states of $^1P^o$ from the first threshold energy -2 a.u. to -1.5 a.u. The middle $1s\epsilon p\ ^1P^o$ includes the $1s\epsilon p$ from -1.5 to -1 a.u. Further, the high $1s\epsilon p\ ^1P^o$ consists of the $1s\epsilon p$ from -1 to -0.5 a.u., which include all of the $2lnl'\ ^1P^o$ resonances. Of these calculated results, the $\mathscr{B}$ parameter without the low $1s\epsilon p$ is closest to the FBA result. The $\mathscr{B}$ value excluding the high $1s\epsilon p$ is closest to the CC result, even though it contains the doubly excited resonances. The $\mathscr{A}$ parameters for the three cases almost coincide with each other and are between the CC and the FBA results. This means that the $1s\epsilon p$ continuum states affect the excitation process to the $(2p)^2\ ^1D^e$ most strongly, and in particular the low energy part is the most important among the $1s\epsilon p$ continuum states. The relative unimportance of the high-energy continuum states is because the background contributions decrease rapidly with increase of emission energy. To summarize, the early excitation process of $He^{**}(N=2)$ from the ground state of He proceeds via the dipole allowed intermediate discrete states $1snp$ and low-lying continuum states $1s\epsilon p$. This point was not recognized by Martín and Salin [5].

IV. SUMMARY AND CONCLUSIONS

We have studied the electron emission spectra of He decaying to $He^+(1s)$ in the $N=2$ and 3 manifolds by fast proton and antiproton impact using the hyperspherical wavefunctions. The resonance shape is found to reflect electron-electron correlation patterns of He. The resonances belonging to the same set of correlation quantum numbers are seen to have similar resonance profiles.

We have compared our absolute EECS with the experimental data for proton impact in the energy range of 1.5 to 3

MeV. Overall, the cross sections are in good agreement with experiment. We have suggested that higher angular configurations as well as high total angular momentum might improve the angle dependence of the theoretical background cross sections. There still remains a small but nonnegligible discrepancy which may be related to the PCI effect in the resonance shape of the $2s2p\ ^1P^o$ state at 2 MeV. Further analysis of this discrepancy seems particularly important, but it lies beyond the scope of the present treatment.

Comparing the CC and FBA results, the excitation mechanism has been investigated. The low-lying continuum states as well as the excited bound states are found to be important intermediate states for excitation to the $(2p)^2\ ^1D^e$ states. We will report the excitation mechanism as well as its dependence on the incident ion's charge sign for the higher $N=3$ manifolds in a separate article including an investigation of a slow electron ejection from low-lying manifolds.

ACKNOWLEDGMENTS

We would like to thank Dr. J. P. Giese and Dr. A. Bordenave-Montesquieu for providing us with their experimental data. The work reported in this paper was partly supported by Grants-in-Aid for Scientific Research on Priority Areas ''Theory of Chemical Reaction—Computational Approach'' and ''Atomic Physics of Multicharged ions'' from the Ministry of Education, Science and Culture of Japan.

[1] T. Morishita, K. Hino, S. Watanabe, and M. Matsuzawa, J. Phys. B **27**, L287 (1994).
[2] F. Martín and A. Salin, J. Phys. B **27**, L715 (1994).
[3] H. Bachau, M. Bahri, F. Martín, and A. Salin, J. Phys. B **24**, 2015 (1991); **25**, 1103E (1992).
[4] H. A. Slim, B. H. Bransden, and D. R. Flower, J. Phys. B **26**, L159 (1993).
[5] F. Martín and A. Salin, J. Phys. B **28**, 639 (1995).
[6] W. Fritsch and C. D. Lin, Phys. Rev. A **41**, 4776 (1990).
[7] K. Moribayashi, K. Hino, M. Matsuzawa, and M. Kimura, Phys. Rev. A **44**, 7234 (1991); **45**, 7922 (1992); **46**, 1684 (1992).
[8] J. O. P. Pedersen and P. Hvelplund, Phys. Rev. Lett. **62**, 2373 (1989).
[9] J. P. Giese, M. Schulz, J. K. Swenson, H. Shöne, M. Benhenni, S. L. Varghese, C. R. Vane, P. F. Dittner, S. M. Shafroth, and S. Datz, Phys. Rev. A **42**, 1231 (1990).
[10] A. Bordenave-Montesquieu, A. Gleizes, P. Moretto-Capelle, S. Andriamonje, P. Benoit-Cattin, F. Martín and A. Salin, J. Phys. B **25**, L367 (1992); **27**, 633E (1994).
[11] A. Bordenave-Montesquieu, P. Moretto-Capelle, A. Gleizes, S. Andriamonje, F. Martín, and A. Salin, J. Phys. B **28**, 653 (1995).
[12] M. E. Rudd, L. H. Toburen, and N. Stolterfoht, At. Data Nucl. Data Tables **18**, 413 (1976).
[13] L. H. Andersen, P. Hvelplund, H. Knudsen, S. P. Møller, K. Elsener, K. -G. Rensfelt, and E. Uggerhøj, Phys. Rev. Lett. **57**, 2147 (1986).
[14] J. F. Reading and A. L. Ford, Phys. Rev. Lett. **58**, 543 (1987).
[15] B. W. Shore, Rev. Mod. Phys. **39**, 439 (1967).
[16] J. Z. Tang, S. Watanabe, and M. Matsuzawa, Phys. Rev. A **46**, 2437 (1992); **46**, 3758 (1992).
[17] J. Z. Tang, S. Watanabe, M. Matsuzawa, and C. D. Lin, Phys. Rev. Lett. **69**, 1633 (1992).
[18] Labeling doubly excited states by the conventional configuration symbols is known to be inadequate. It is more appropriate to use correlation quantum numbers, $N(K,T)^A n$. Here K and T pertain to the angular correlation; cf. D. R. Herrick and O. Sinanoğlu, Phys. Rev. A **11**, 97 (1975) and D. R. Herrick, *ibid.* **12**, 413 (1975). The principal quantum number N of the inner electron defines a series of resonances that converges to the He $^+$(N) threshold and the radial quantum number n of the outer electron takes on different values $n \geqslant N$. The symbol A pertains to the radial correlations; cf. C. D. Lin, Adv. At. Mol. Phys. **22**, 77 (1986). Resonant states with $A=+$ tend to have large probability densities where $r_1=r_2$, whereas those with $A=-$ have small probability densities there. The case $A=0$ means that the states are classifiable with neither + nor −. For historical reasons we retain the conventional notation in this work, though we discourage its continued use.
[19] C. L. Pekeris, Phys. Rev. **112**, 1649 (1958); **126**, 1470 (1962); **127**, 509 (1962); B. Shiff, H. Lifson, C. L. Pekeris, and P. Rabinowitz, *ibid.* **140**, A1104 (1965).
[20] L. C. Green, E. K. Kolshin, and N. C. Johnson, Phys. Rev. **139**, A373 (1965).
[21] Y. K. Ho and J. Callaway, Phys. Rev. A **23**, 2137 (1981).
[22] Y. K. Ho and J. Callaway, J. Phys. B **18**, 3481 (1985).
[23] D. H. Oza, Phys. Rev. A **33**, 824 (1985).
[24] K. Hino, M. Nagase, H. Okamoto, T. Morishita, M. Matsuzawa, and M. Kimura, Phys. Rev. A **49**, 3753 (1994).
[25] M. J. Seaton, *Atomic and Molecular Processes*, edited by D. R. Bates (Academic Press, New York, 1962), pp. 374–420.
[26] Their projection operator technique of [5] makes it possible to separate the contribution to the Shore parameters from various partial waves.
[27] J. P. Giese (private communication).
[28] Figure 5 of [11] is incorrectly produced. The general features of the cross sections available in preprint form are very similar to our figure.
[29] V. V. Balashov, S. S. Lipovetskiĭ, and V. S. Senashenko, Zh. Eksp. Teor. Fiz. **63**, 1622 (1972) [Sov. Phys. JETP **36**, 858 (1973)].
[30] A. L. Godunov, Sh. D. Kunikeev, N. V. Novikov, and V. S. Senashenko, Zh. Eksp. Teor. Fiz. **96**, 1638 (1989) [Sov. Phys. JETP **69**, 927 (1989)].
[31] A. L. Godunov, N. V. Novikov, and V. S. Senashenko, J. Phys. B **23**, L359 (1990); **25**, L43 (1992).
[32] P. W. Arcuni and D. Schneider, Phys. Rev. A **36**, 3059 (1987).
[33] The importance of charge-transfer channels at low-impact energy < 150 keV is noted in the recent work by; cf. H. A. Slim, B. H. Bransden, and D. R. Flower, J. Phys. B **28**, 1623 (1995). No systematic study is known for high-impact energies.